CrossMark
click for updates

First principles thermodynamical modeling of the binodal and spinodal curves in lead chalcogenides†

Demet Usanmaz,[ab] Pinku Nath,[ab] Jose J. Plata,[ab] Gus L. W. Hart,[bc] Ichiro Takeuchi,[bde] Marco Buongiorno Nardelli,[bf] Marco Fornari[bg] and Stefano Curtarolo*[bh]

High-throughput *ab initio* calculations, cluster expansion techniques, and thermodynamic modeling have been synergistically combined to characterize the binodal and the spinodal decompositions features in the pseudo-binary lead chalcogenides PbSe–PbTe, PbS–PbTe, and PbS–PbSe. While our results agree with the available experimental data, our consolute temperatures substantially improve with respect to previous computational modeling. The computed phase diagrams corroborate that in *ad hoc* synthesis conditions the formation of nanostructure may occur justifying the low thermal conductivities in these alloys. The presented approach, making a rational use of online quantum repositories, can be extended to study thermodynamical and kinetic properties of materials of technological interest.

[a] *Department of Mechanical Engineering and Materials Science, Duke University, Durham, North Carolina 27708, USA*

[b] *Center for Materials Genomics, Duke University, Durham, NC 27708, USA*

[c] *Department of Physics and Astronomy, Brigham Young University, Provo, Utah 84602, USA*

[d] *Center for Nanophysics and Advanced Materials, University of Maryland, College Park, Maryland 20742, USA*

[e] *Department of Materials Science and Engineering, University of Maryland, College Park, Maryland 20742, USA*

[f] *Department of Physics and Department of Chemistry, University of North Texas, Denton TX, USA*

[g] *Department of Physics and Science of Advanced Materials Program, Central Michigan University, Mount Pleasant, MI 48858, USA*

[h] *Materials Science, Electrical Engineering, Physics and Chemistry, Duke University, Durham NC, 27708 USA. E-mail: stefano@duke.edu; Fax: +1-919-660-8963; Tel: +1-919-660-5506*

† Electronic supplementary information (ESI) available. See DOI: 10.1039/c5cp06891f

1 Introduction

For decades, the physical properties of lead chalcogenides have generated substantial interest in a number of fields, in particular for applications in semiconductor technology.[1] PbS, PbSe, and PbTe have distinct structural and electronic properties compared to III–V and II–VI compounds. These include high carrier mobilities, narrow band gaps with negative pressure coefficients, high dielectric constants, and a positive temperature coefficient.[2–4] In addition, PbS, PbSe, and PbTe were predicted to be weak topological insulators, with a band inversion observed at the N point of the distorted body-centered tetragonal Brillouin zone.[5] These important and varied properties have allowed lead chalcogenides to be used extensively in optoelectronic devices such as lasers and detectors, thermophotovoltaic energy converters, and thermoelectric materials.[1,6–10]

As thermoelectric materials, lead chalcogenides may exhibit electrical conductivities, σ, in excess of $2–4 \times 10^{-4}\ \Omega^{-1}\ cm^{-1}$, thermopowers, S, around $150\ \mu V\ K^{-1}$, and thermal conductivities, κ, on the order of $1–2\ Wm^{-1}\ K^{-1}$. This leads to figures of merit $ZT = \sigma S^2/\kappa$ larger than 1 at high temperatures, T. Such outstanding performances are due on the details of the electronic structure,[11–15] and on the ability to dramatically reduce the thermal conductivity with alloying and nanostructuring.[16–19] While pure lead chalcogenides are attractive on their own, their alloys are even more interesting. The appeal arises from their mechanical and electronic tunability, which can be optimized for specific technological needs.[20–22] For example, the $PbTe_{1-x}Se_x$ pseudo-binary system has a higher ZT value than its corresponding binary forms.[23,24] Thallium doping in PbTe causes changes in the electronic density of states, increasing the ZT value to 1.5 at 773 K.[11] Similarly, a ZT of 1.3 at 850 K was reported for aluminum doped PbSe.[25] Furthermore, $Pb_{9.6}Sb_{0.2}Te_{10-x}Sb_x$ is known to exhibit lower thermal conductivity and a higher ZT than $PbSe_{1-x}Te_x$.[26] This is also true for nanostructured $(Pb_{0.95}Sn_{0.05}Te)_{0.92}(PbS)_{0.08}$, as the low thermal conductivity leads to a $ZT = 1.5$ at 642 K.[27] The properties of this group of pseudo-binaries depend greatly on the atomic details of the material's morphology. This can be partially understood in terms of thermodynamical features. The excellent thermoelectric performances, for example, were tentatively ascribed to the limited miscibility of the components. This gives rise to

structural inhomogeneities that lower the thermal conductivity without damaging the electronic transport.[19] Such control over the morphology could be also used to optimize functionalities associated with topological effects.

In this work we study the phase diagram of lead chalcogenide pseudo-binaries. We predict quantitatively the boundary of the solid solution (the binodal curve that defines the region of miscibility), as well as the spinodal region. These features are key for rationalizing and honing synthesis and characterization of optimized systems. To the best of our knowledge, our study is the first to completely and accurately reports such characterization. The phase diagram is essential for properly establishing manufacturing processes. There has been only one previous attempt to model phase diagrams of lead chalcogenides using thermodynamic modeling (TM),[28] which predicted consolute temperature (T_c) values far from those reported in experimental studies.[29] The disagreement was attributed to the difficulty of an exhaustive exploration of all the possible structural configurations for each composition. This difficulty can be rectified by using the cluster expansion (CE) technique which is a well known method to investigate the energetics of various materials.[30–33] Here, we built upon the synergy between cluster expansion (CE) techniques, high-throughput (HT) *ab initio* calculations,[32,34,35] and thermodynamical modeling to find acceptable agreement between our Monte Carlo simulations (MC) and the available experimental results.

2 Methodology

2.1 Thermodynamic modeling

Pseudo-binary systems are represented by the formula $(A_{x_A}B_{x_B})_aC_c$ (or $A_xB_{1-x}C$) with mole fractions x_A and x_B of elements A and B respectively, related by $x_A + x_B = 1$. The small letters a and c represent number of sites per formula.[36,37] The Gibbs energy of such iso-structural pseudo-binary systems can be written as:[36,37]

$$G_{(A,B)_aC_c} = x_AG_{A_aC_c} + x_BG_{B_aC_c} + k_BT(x_A\ln(x_A) + x_B\ln(x_B)) + x_Ax_BL_{A,B:C}$$
(1)

where $G_{A_aC_c}$ and $G_{B_aC_c}$ represent the Gibbs free energy of A_aC_c and B_aC_c materials. These two variables can be computed at any temperature by fitting available experimental data[38] to the polynomial form[39] shown in eqn (2):

$$G(T) = a + bT + cT\ln T + dT^2 + eT^{-1} + fT^3.$$
(2)

The third term in the eqn (1) is the entropy of mixing, and the last term is the excess energy of mixing that parameter can take negative or positive values. If $L_{A,B:C}$ is negative, it indicates that the system tends to create a solid solution. A positive value of $L_{A,B:C}$ indicates a repulsive interaction between phases, penalizing formation of intermediate alloys. To find the excess mixing energy, the composition-dependent interaction parameter $L_{A,B:C}$ can be calculated with eqn (3):

$$\Delta H = x_Ax_BL_{A,B:C}.$$
(3)

The enthalpy of formation, ΔH, is defined as:

$$\Delta H = E_{(A,B)_aC_c} - x_AE_{A_aC_c} - x_BE_{B_aC_c},$$
(4)

where $E_{(AB)_aC_c}$, $E_{A_aC_c}$, and $E_{B_aC_c}$ are the total energies of compounds $(AB)_aC_c$, A_aC_c and B_aC_c, respectively. These energies can be found from the fully relaxed structures using density functional theory (DFT).

A combination of high throughput *ab initio* calculations and thermodynamic modelling are used to predict the interaction parameter, $L(x)$.[39–41] The result is a zero temperature approximation of the actual value. The most common method to describe the composition dependent interaction parameter is the Redlich–Kister equation,[36,37,42] where the interaction parameter is written in a polynomial form:

$$L(x) = \sum_{i=0}^{n} L_i(x_A - x_B)^n.$$
(5)

We fit this polynomial to the formation enthalpy data obtained from DFT and/or CE calculations. We checked that an $n = 2$ polynomial is enough to obtain a good fit to the data, so that only L_0, L_1, and L_2 need to be determined:

$$L(x) \simeq L_0 + xL_1 + x^2L_2$$
(6)

to compute the interaction parameter.

The main computational challenge lies in characterizing many configurations for many compositions. Some authors have attempted to address the issue, by generating, few configurations and/or few compositions which is computationally really demanding[28,39–41] Here, we challenged the problem more drastically: by relying on the advantages of a hybrid cluster expansion (CE)- high throughput approach[43] which features an exhaustive exploration of different configurations for all the different compositions. Cluster expansion is widely used to describe phase diagrams, in which A and B belong to the same sublattice, by making the exploration of multiconfigurational space computationally affordable.[32,44,45] The automatic generation of hundreds or thousands of configurations for whole composition range and the prediction of their energy only computing some tens of DFT structures make CE the ideal and most reliable in lattice technique to avoid a large set of DFT supercell calculations. The computational efficiency was achieved with HT methods,[43,46] and rational use of online repositories (AFLOWLIB.org).[47]

2.2 Cluster expansion

In the cluster expansion technique, the configurational energy of an alloy as written as a sum of many-body occupation variables $\{\sigma\}$:[48]

$$E(\sigma) = J_0 + \sum_i J_i\sigma_i + \sum_{ij} J_{ij}\sigma_{ij} + \dots,$$
(7)

where J_0, J_i, J_{ij}, *etc.* are known as effective cluster interactions and must be determined.

The above equation can be rewritten into symmetrically distinct sets of clusters, α:

$$E(\sigma) = \sum_\alpha m_\alpha J_\alpha \left\langle \prod_{i \in \alpha} \sigma_i \right\rangle,$$
(8)

where m_α represents symmetrically equivalent clusters α in a given reference volume.[30] The J_α parameters are obtained by fitting a relatively small number of DFT calculated energies.

The reliability of the predicted energy may be determined using the cross-validation score CV:

$$(\text{CV})^2 = \frac{1}{N} \sum_{S=1}^{N} \left(E_S - \hat{E}_S \right)^2, \qquad (9)$$

where E_S represents the calculated energies from DFT and $\hat{E}_S$ is the predicted energies from CE. A small CV score guarantees that CE predicted energies are in agreement with DFT computed energies. The enumeration of configurations, calculation of the effective interaction parameters, determination of ground state structures, and prediction of more structures was performed with the Alloy Theoretic Automated Toolkit (ATAT).[49] Calculated phase diagrams were obtained with Monte Carlo (MC) simulations performed with phb code. The algorithm automatically follows a given phase boundary and is provided by the ATAT package.[49–51]

2.3 High-throughput *ab initio* calculations

All DFT calculations were carried out by using the Automatic-Flow for Materials Discovery (AFLOW)[47,52,53] and DFT Vienna ab initio simulation program (VASP).[54] Calculations were performed using AFLOW standards.[55] We use the projector augmented wave (PAW) pseudopotentials[56] and the exchange and correlation functionals parametrized by the generalized gradient approximation proposed by Perdew–Burke–Ernzerhof.[57] All calculations use a high energy-cutoff, which is 40% larger than the maximum cutoff of all pseudopotentials used. Reciprocal space integration was performed using 8000 k-points per reciprocal atom. Spin–orbit coupling was not treated in the calculations due to its minimal influence in ΔH (smaller than 1.5 meV per atom). Structures were fully relaxed (cell volume and ionic positions) such that the energy difference between two consecutive ionic steps was smaller than 10^{-4} eV.

PbS, PbSe and PbTe crystallize in the NaCl structure and belong to the $Fm\bar{3}m$ space group (# 225). We used the bulk primitive cell (2 atoms per cell) as input for the cluster expansion calculations. The number of atoms for each configuration depend on the alloy concentration, x, however, supercells of 20 atoms were chosen as the limit size for structures generated by ATAT package.

For each system, we used 100 DFT calculated energies and 250 CE predicted energies for 19 different compositions. While the number of DFT calculation is based on obtaining a CV score below 5 meV, the number of predicted energies was converged until no significance changes were observed in the consolute temperature of the systems (see Fig. S1, ESI†). This exhaustive multiconfigurational screening is the main difference compared with previous studies for this systems.[28] Space and point group symmetries of intermediate composition structures were determined using AFLOW.

3 Results and discussions

3.1 The PbSe$_{1-x}$Te$_x$ alloy

In agreement with experimental data, we found that PbSe and PbTe are immiscible systems at 0 K. This is shown in Fig. 1(a), where formation enthalpies are positive for all compositions ($0 < x < 1$). The CE predicted energies ($\square$) are in excellent agreement with DFT calculated structures ($\bigcirc$) providing a cross validation score of 4×10^{-4}. Eqn (3) is used to fit the interaction parameters L_0, L_1, L_2 to the highly symmetric
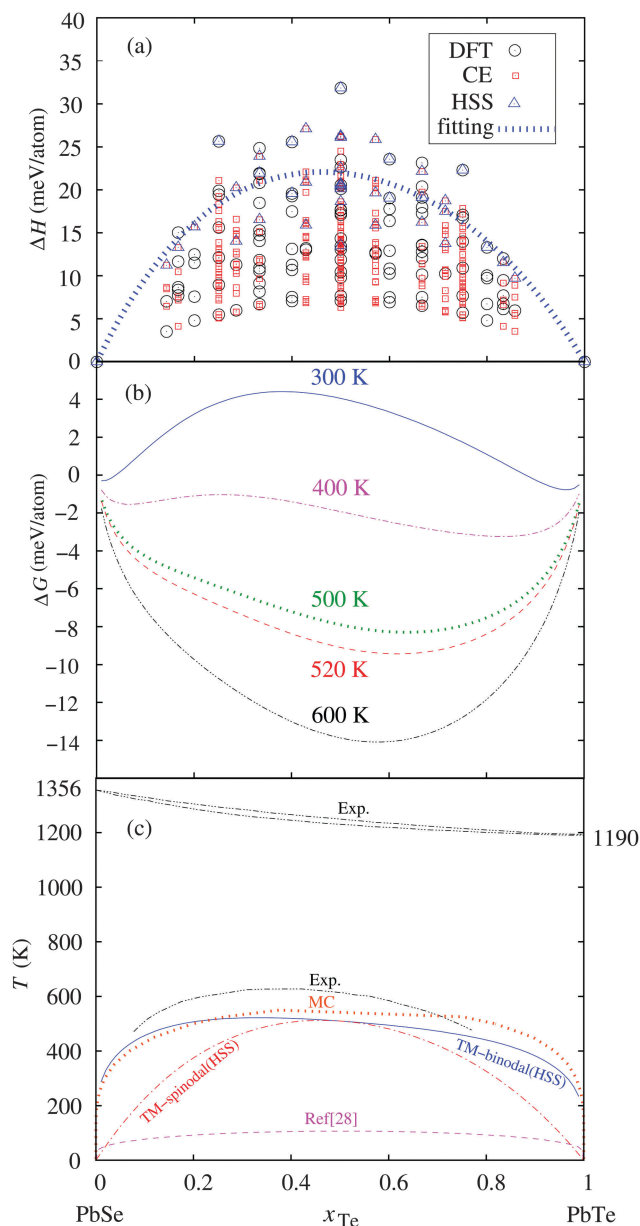

Fig. 1 (a) Formation enthalpies of the PbSe–PbTe structures using DFT calculations ($\bigcirc$) and CE technique ($\square$). Highly symmetric structures are represented by $\triangle$ and the fitting of these points to obtain the interaction parameter is plotted with a blue dashed line. (b) $\Delta G(x)$ diagram at various temperatures. (c) Binodal and spinodal curves from TM (—— and — · —), and MC simulations (· · ·), compared with experimental data[29] (– · · · –) and the previous theoretical model (- - -) from Boukhris *et al.*[28]

structures (HSS)[58,59] included HSS have a larger degeneracy and thus greater weight in the properties of the ensemble; particularly at high temperatures. In order to emphasize the importance of HSS with respect to other structures that contribute with a smaller weight, we computed interaction parameters by averaging over the whole data set (see Fig. S3(b), ESI†). This approach drastically decreases the consolute temperature (346 K) and it is far from experimental or MC results and closer to previous theoretical results.[28] These effects may be ascribed to an incorrect averaging methods that does not take into account properly the weight of the HSS with respect to the other structures. The comparison with experimental data demonstrate the relevance of the HSS and their large contribution to the properties of the alloy.

Our quantitative results confirm the Hume–Rothery rules.[60] These rules qualitatively predict the miscibility of two metals based on four properties: atomic radius, crystal lattice, valence and electronegativity. Amongst the chalcogens, the atomic radius changes from 1.04 Å in S, to 1.17 Å in Se, to 1.37 Å in Te. These size variations create a mismatch between the lattice parameters of PbTe and PbSe, causing incoherence in the interface and phase decomposition, eventually. $\Delta G(x)$ diagrams at different temperatures are plotted in Fig. 1(b). It can be seen the ΔG function has two minima and a single maximum at low temperatures. At high temperatures close to T_c, it becomes convex, with one minimum.

The binodal curve $T_c(x)$ is defined by the horizontal tangent points of the Gibbs free energy, G. When $T < T_c$, the alloy starts decomposing. Additionally, our calculations let us determine the spinodal curve that discriminates metastable and unstable regions in the pseudo-alloy phase diagram. The spinodal curve is the locus of the points where the second derivative of G is equal to 0:

$$\frac{\partial^2 G_{(AB)_a C_c}}{\partial x^2} = 0. \tag{10}$$

We computed first and second derivatives of the Gibbs free energy within our thermodynamical model. In order to obtain the L_0, L_1, L_2 that are necessary to compute $L(x)$ at any composition, we use HSS to fit eqn (3). After computing the L_n constants, $\Delta G_{(Se,Te)_a Pb_c}$ is obtained via eqn (1). The results obtained from the thermodynamic model are compared with our MC results, previous theoretical predictions,[28] and experimental data.[29,61]

Our calculations encompass the entire range of concentrations, and reproduce the asymmetry observed experimentally in the binodal curve. In order to quantitatively compare all data, we analyzed the consolute temperature or upper critical solution temperature (T_c) describing the lowest temperature at which both phases are miscible at any composition. Experimentally PbSe$_{1-x}$Te$_x$ alloy presents, at $x = 0.4$, a T_c closer to 623 K.[29,61] This quantity is far from the value predicted by Boukhris et al.,[28] which is around 106 K. The consolute temperature predicted by our thermodynamic model at 520 K (16.5% error) is around $x = 0.34$ (see Fig. 1(c)). Our results quantitatively improve the prediction of T_c with of Boukhris et al.[28] because of the exhaustive multiconfigurational exploration allowed by CE technique.

We emphasize that the CE approximation only reduces the computational cost of the method, making it more affordable for a wider exploration of the multiconfigurational space (see Fig. S2, ESI†). Moreover, this value approaches the results obtained by much more expensive techniques such as MC, in which we obtain a value close to 550 K (11.7% error). Discrepancies between MC and TM at larger Te (Se) concentrations arise from difficulties in converging MC calculations in the dilute limit of Se (Te).

The experimental miscibility gap presents a slight asymmetric form that is reproduced by MC and our TM. This asymmetry is observed in experiments, but was not seen in previous theoretical work.[28] This phenomenon will be discussed in the next section.

In contrast to the binodal curve, the spinodal curve is quite symmetric. The combination of the symmetric spinodal and asymmetric binodal curves at the Se-rich region causes nucleation of PbSe$_{1-x}$Te$_x$ at higher temperatures and nucleation cause a Se-rich nano-structuring. This information is very important for fine tuning synthesis protocols to obtain the desired morphologies.

3.2 The PbS$_{1-x}$Te$_x$ alloy

The atomic radius of Te is 24% larger than the S radius. Thus, the PbS–PbTe system follows the same trend as PbSe–PbTe, and they are immiscible at 0 K.

Our ΔH values are greater than 0 eV for the whole range of concentrations (see Fig. 2(a)). CE predicted energies are again in agreement with DFT calculations, obtaining a CV score of about 3×10^{-3}. The fitting for $L(x)$ is also depicted in Fig. 2(a) using highly symmetric points. Similarly to PbSe–PbTe, the ΔG function changes to a convex shape at high temperatures (Fig. 2(b)).

The calculated phase diagram of the PbS$_{1-x}$Te$_x$ alloy is shown in Fig. 2(c). Experimental results show again a slight asymmetry with a maximum around $x = 0.3$. This is in agreement with our results, while MC simulations fail to show this asymmetry. The predicted consolute temperatures for PbS–PbTe follow the same trend as PbSe–PbTe. Results published by Boukhris et al.[28] considerably underestimate the experimental value for T_c (1083 K). Our prediction of the consolute temperature is slightly larger than experiments;[29] being 1385 and 1365 K using MC simulations and TM, respectively. As seen from Fig. 1(c) and 2(c) PbSe–PbTe and PbS–PbTe systems show a very similar trend of a slightly asymmetric spinodal curve, and considerably asymmetric binodal curve. This trend shows that formation of the Te-rich alloy starts at lower temperatures than Se-rich compositions.

3.3 The PbS$_{1-x}$Se$_x$ alloy

Our methodology was also applied to the PbS–PbSe system. All positive energies in Fig. 3 indicate that PbS and PbSe systems are not miscible at 0 K. As far as we know, there are no experimental data available below 573 K for this system.[61] However, it has been shown that MC simulations predict the T_c for different systems quite well, and can describe the miscibility gap.[30,31] For this alloy, thermodynamic modelling predicts a T_c slightly below 200 K and MC predicts a T_c slightly lower than 250 K.
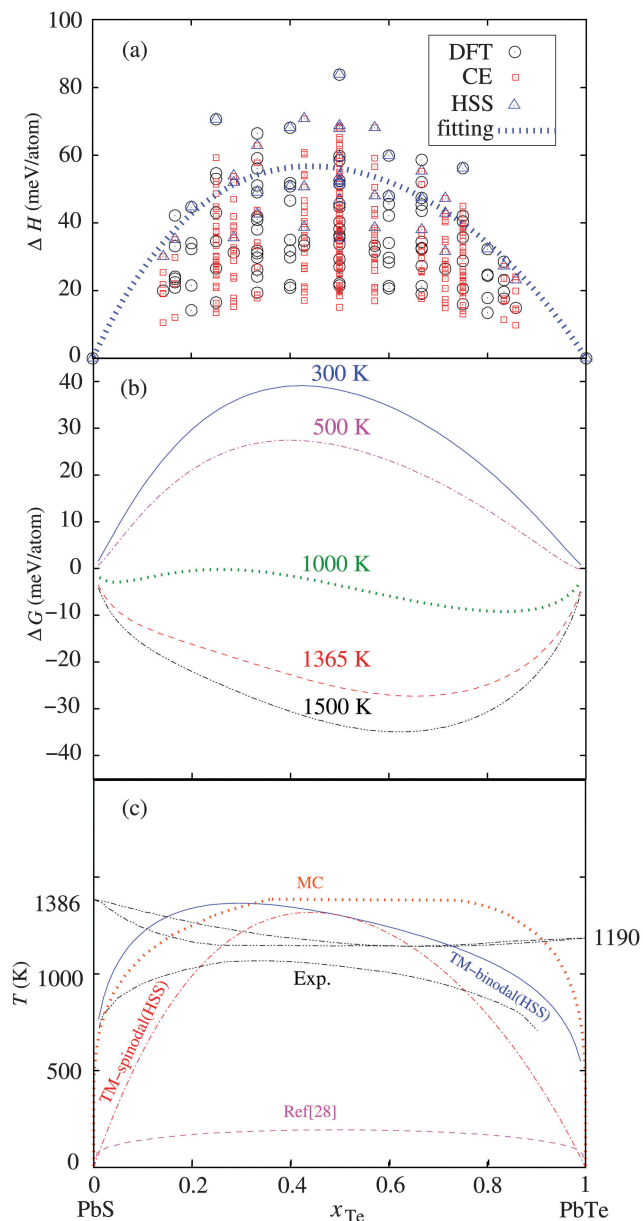
Fig. 2 (a) Formation enthalpies of the PbS–PbTe structures using DFT calculations (○) and CE technique (□). Highly symmetric structures are represented by △ and the fitting of these points to obtain the interaction parameter is plotted with a blue dashed line. (b) $\Delta G(x)$ diagram at various temperatures. (c) Binodal and spinodal curves from TM (—— and – · –), and MC simulations (···), compared with experimental data[29] (– · · · –) and the previous theoretical model (- - -) from Boukhris et al.[28]
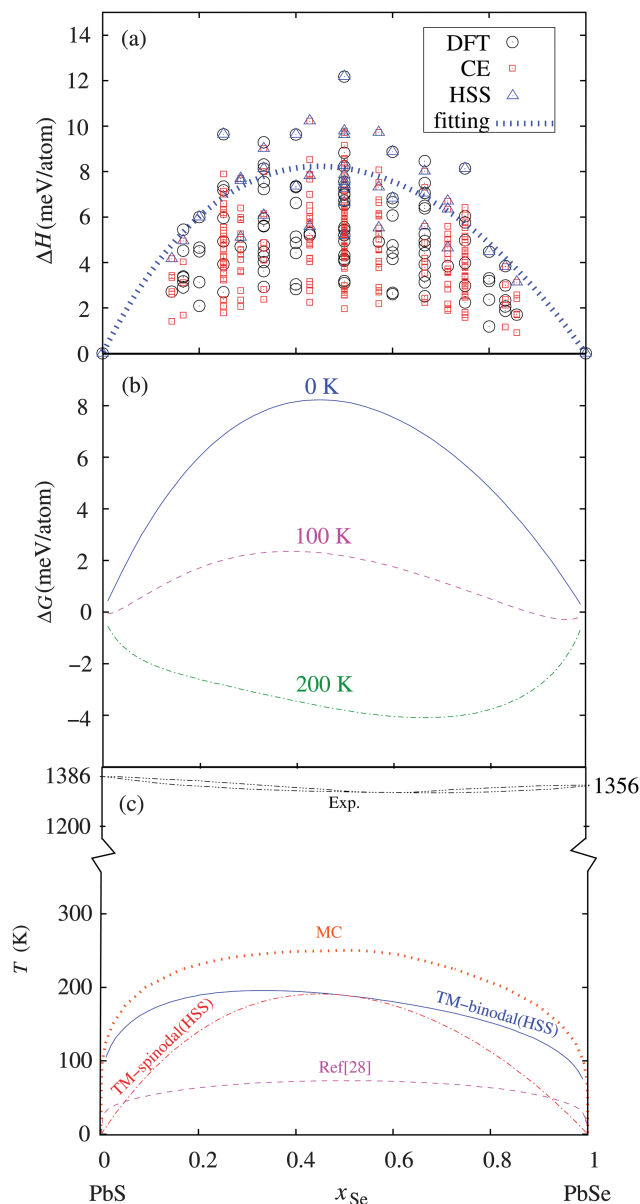

Fig. 3 (a) Formation enthalpies of the PbS–PbSe structures using DFT calculations (○) and CE technique (□). Highly symmetric structures are represented by △ and the fitting of these points to obtain the interaction parameter is plotted with a blue dashed line. (b) $\Delta G(x)$ diagram at various temperatures. (c) Binodal and spinodal curves from TM (—— and – · –), and MC simulations (···), compared with experimental data[29] (– · · · –) and the previous theoretical model (- - -) from Boukhris et al.[28]

3.4 General considerations

The lattice mismatch between the two solids (PbS, PbSe, or PbTe) is a good descriptor to analyze the trends observed experimentally (see Fig. 4). Lattice mismatch, ε, is defined as:

$$\varepsilon = \frac{\left(a_{(A,B)_a C_c} - a_{\text{solvent}} \right)}{a_{\text{solvent}}} \times 100, \qquad (11)$$

where $a_{(A,B)_a C_c}$ denotes the lattice constant of intermediate alloys and a_{solvent} is the lattice constant of the most abundant

binary alloy. There is a correlation between the lattice mismatch of the alloy, ΔH, and the consolute temperature. The higher the mismatch, the higher ΔH becomes and thus, a higher T_c is obtained. For instance, the larger mismatch corresponds to the PbS–PbTe system, which presents a maximum enthalpy of formation at $x = 0.5$, with 80 meV per atom and a T_c of 1083 K. For the PbSe–PbTe system, the maximum ΔH is around 22 meV per atom and the consolute temperature is 623 K. Following this trend, PbS–PbSe system presents a smaller mismatch and a smaller ΔH 8 meV per atom. Thus, a consolute temperature
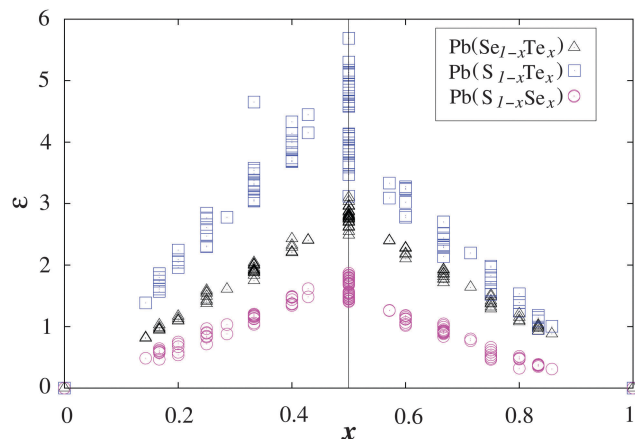
Fig. 4 Lattice mismatch for lead chalcogenides alloys. For each ternary system we consider 0 mismatch when $x = 0$.

smaller than 623 K is expected. If we approximate this correlation to a linear function, for a lattice mismatch around 3% we get a T_c close to 270 K; which is in agreement with MC and our thermodynamic model results.

Mismatch between lattices can be also used to explain the asymmetry of the binodal curves. We can define the asymmetry of the curve as the ratio between the decomposition temperature of two points equidistant to $x = 0.5$. We have chosen 0.2 and 0.8 to define our asymmetry descriptor, ε_T:

$$\varepsilon_T = \frac{T(x = 0.8)}{T(x = 0.2)}. \tag{12}$$

Using this definition, we can assume that a perfectly symmetric spinodal curve has $\varepsilon_T = 1$.

As discussed above, mismatch between lattices is directly related to the magnitude and size of the spinodal curve. Mismatch is the driving force in the three systems we are studying. Thus, we propose a second asymmetry descriptor, ε_r, based on the ratio between the lattice mismatch at two points equidistant to $x = 0.5$:

$$\varepsilon_r = \frac{\varepsilon(x = 0.8)}{\varepsilon(x = 0.2)}. \tag{13}$$

The asymmetry descriptor values for the three systems are shown in Table 1. ε_T shows PbS–PbSe as the most asymmetric spinodal curve, then PbS–PbTe, and finally the PbSe–PbTe system. This trend is exactly the same for ε_r, emphasizing the importance of the lattice strain in the of these systems. The ability of the method to explore a large configurational space guarantees the correct description of the asymmetry of the binodal curve.

Table 1 Asymmetric descriptors for spinodal curves for lead chalcogenides

	PbSe–PbTe	PbS–PbTe	PbS–PbSe
ε_T	0.86	0.80	0.80
ε_r	0.84	0.59	0.49

4 Conclusions

A hybrid approach, comprising high-throughput *ab initio* and cluster-expansion techniques is used to create a thermodynamic model for calculating binodal and spinodal decompositions in pseudo binary lead chalcogenides (PbSe–PbTe and PbS–PbTe). The model overcomes the limitations of previous theoretical studies, where too few compositions and/or configurations were taken into account. The obtained thermodynamical features are very close to the experimentally data, when available. We also capture the asymmetry of the binodal curve, experimentally observed and previously computationally unresolved. Additionally, phase diagrams for systems without experimental characterization, such as the PbS–PbSe alloy, are suggested. The results have been validated by using MC simulations, and lattice mismatch between the binary solids descriptors.

Overall the approach is suitable for the high-throughput characterization of miscibility gaps, spinodal and other decomposition phenomena.

References

1 D. Khokhlov, *Lead Chalcogenides: Physics and Applications*, Taylor & Francis, Great Britain, 2002.
2 S. Adachi, *Properties of Group-IV, III-V and II-VI Semiconductors*, John Wiley & Sons, England, 2005.
3 T. S. Moss, G. J. Burrell and B. Ellis, *Semiconductor Opto-Electronics*, Butterworth, 1973.
4 Y. I. Ravich, B. A. Efimova and I. A. Smirnov, *Semiconducting Lead Chalcogenides*, Plenum Press, 1970.
5 K. Yang, W. Setyawan, S. Wang, M. Buongiorno Nardelli and S. Curtarolo, *Nat. Mater.*, 2012, **11**, 614–619.
6 A. P. Alivisatos, *Science*, 1996, **271**, 933–937.
7 R. Dalven, in *Solid State Physics*, ed. H. Ehrenreich, F. Seitz and D. Turnbull, Academic Press, New York, 1973, vol. 28, pp. 179–224.
8 Y.-L. Pei and Y. Liu, *J. Alloys Compd.*, 2012, **514**, 40–44.
9 P. Johari and V. B. Shenoy, *ACS Nano*, 2012, **6**, 5449–5456.
10 H. Wang, Y. Pei, A. D. Lalonde and G. J. Snyder, *Adv. Mater.*, 2011, **23**, 1366–1370.
11 J. P. Heremans, V. Jovovic, E. S. Toberer, A. Saramat, K. Kurosaki, A. Charoenphakdee, S. Yamanaka and G. J. Snyder, *Science*, 2008, **321**, 554–557.
12 D. Parker, D. J. Singh, Q. Zhang and Z. Ren, *J. Appl. Phys.*, 2012, **111**, 123701.
13 D. Parker and D. J. Singh, *Phys. Rev. B: Condens. Matter Mater. Phys.*, 2010, **82**, 035204.

14 D. Parker and D. J. Singh, *Solid State Commun.*, 2014, **182**, 34–37.

15 N. A. Mecholsky, L. Resca, I. L. Pegg and M. Fornari, *Phys. Rev. B: Condens. Matter Mater. Phys.*, 2014, **89**, 155131.

16 J. He, J. R. Sootsman, S. N. Girard, J.-C. Zheng, J. Wen, Y. Zhu, M. G. Kanatzidis and V. P. Dravid, *J. Am. Chem. Soc.*, 2010, **132**, 8669–8675.

17 Z.-G. Chen, G. Han, L. Yang, L. Cheng and J. Zou, *Prog. Nat. Sci.*, 2012, **22**, 535–549.

18 T. C. Harman, M. P. Walsh, B. E. Laforge and G. W. Turner, *J. Electron. Mater.*, 2005, **34**, L19–L22.

19 L.-D. Zhao, J. He, S. Hao, C.-I. Wu, T. P. Hogan, C. Wolverton, V. P. Dravid and M. G. Kanatzidis, *J. Am. Chem. Soc.*, 2012, **134**, 16327–16336.

20 A. Zaoui, S. Kacimi, M. Zaoui and B. Bouhafs, *Mater. Chem. Phys.*, 2009, **114**, 650–655.

21 N. Ullah, G. Murtaza, R. Khenata, N. Hassan, S. Naeem, M. N. Khalid and S. B. Omran, *Comput. Mater. Sci.*, 2014, **83**, 496–503.

22 S. A. Yamini, H. Wang, Z. M. Gibbs, Y. Pei, S. X. Dou and G. J. Snyder, *Phys. Chem. Chem. Phys.*, 2014, **16**, 1835–1840.

23 Q. Zhang, F. Cao, W. Liu, K. Lukas, B. Yu, S. Chen, C. Opeil, D. Broido, G. Chen and Z. Ren, *J. Am. Chem. Soc.*, 2012, **134**, 10031–10038.

24 Y. Pei, X. Shi, A. LaLonde, H. Wang, L. Chen and G. J. Snyder, *Nature*, 2011, **473**, 66–69.

25 Q. Zhang, H. Wang, W. Liu, H. Wang, B. Yu, Q. Zhang, Z. Tian, G. Ni, S. Lee, K. Esfarjani, G. Chen and Z. Ren, *Energy Environ. Sci.*, 2012, **5**, 5246–5251.

26 P. F. P. Poudeu, J. DAngelo, H. Kong, A. Downey, J. L. Short, R. Pcionek, T. P. Hogan, C. Uher and M. G. Kanatzidis, *J. Am. Chem. Soc.*, 2006, **128**, 14347–14355.

27 J. Androulakis, C.-H. Lin, H.-J. Kong, C. Uher, C.-I. Wu, T. Hogan, B. A. Cook, T. Caillat, K. M. Paraskevopoulos and M. G. Kanatzidis, *J. Am. Chem. Soc.*, 2007, **129**, 9780–9788.

28 N. Boukhris, H. Meradji, S. Ghemid, S. Drablia and F. E. H. Hassan, *Phys. Scr.*, 2011, **83**, 065701.

29 H. Liu and L. L. Y. Chang, *Mineral. Mag.*, 1994, **58**, 567–578.

30 B. P. Burton and A. van de Walle, *Chem. Geol.*, 2006, **225**, 222–229.

31 B. P. Burton, S. Demers and A. van de Walle, *J. Appl. Phys.*, 2011, **110**, 023507.

32 O. Levy, G. L. W. Hart and S. Curtarolo, *J. Am. Chem. Soc.*, 2010, **132**, 4830–4833.

33 N. A. Zarkevich, T. L. Tan and D. D. Johnson, *Phys. Rev. B: Condens. Matter Mater. Phys.*, 2007, **75**, 104203.

34 O. Levy, R. V. Chepulskii, G. L. W. Hart and S. Curtarolo, *J. Am. Chem. Soc.*, 2010, **132**, 833–837.

35 R. H. Taylor, S. Curtarolo and G. L. W. Hart, *J. Am. Chem. Soc.*, 2010, **132**, 6851–6854.

36 N. Saunders and A. P. Miodownik, *CALPHAD: A Comprehensive Guide*, Elsevier Science, UK, 1998.

37 M. Hillert, *Phase Equilibria, Phase Diagrams and Phase Transformations: Their Thermodynamic Basis*, Cambridge University Press, UK, 2007.

38 I. Barin, *Thermochemical Data of pure substances*, VCH, Germany, 1993.

39 R. F. Zhang and S. Verpek, *Acta Mater.*, 2007, **55**, 4615–4624.

40 S. H. Sheng, R. F. Zhang and S. Verpek, *Acta Mater.*, 2011, **59**, 297–307.

41 S. H. Sheng, R. F. Zhang and S. Verpek, *Acta Mater.*, 2011, **59**, 3498–3509.

42 O. Redlich and A. T. Kister, *Ind. Eng. Chem.*, 1948, **40**, 345–348.

43 S. Curtarolo, G. L. W. Hart, M. Buongiorno Nardelli, N. Mingo, S. Sanvito and O. Levy, *Nat. Mater.*, 2013, **12**, 191–201.

44 S. V. Barabash, V. Ozolins and C. Wolverton, *Phys. Rev. Lett.*, 2008, **101**, 155704.

45 J. Z. Liu and A. Zunger, *Phys. Rev. B: Condens. Matter Mater. Phys.*, 2008, **77**, 205201.

46 W. Setyawan and S. Curtarolo, *Comput. Mater. Sci.*, 2010, **49**, 299–312.

47 S. Curtarolo, W. Setyawan, S. Wang, J. Xue, K. Yang, R. H. Taylor, L. J. Nelson, G. L. W. Hart, S. Sanvito, M. Buongiorno Nardelli, N. Mingo and O. Levy, *Comput. Mater. Sci.*, 2012, **58**, 227–235.

48 D. de Fontaine, *Solid State Physics*, New York, 1994, pp. 33–176.

49 A. van de Walle, M. Asta and G. Ceder, *Calphad*, 2002, **26**, 539–553.

50 A. van de Walle and G. Ceder, *J. Phase Equilib.*, 2002, **23**, 348–359.

51 A. van de Walle and M. Asta, *Modell. Simul. Mater. Sci. Eng.*, 2002, **10**, 521.

52 S. Curtarolo, W. Setyawan, G. L. W. Hart, M. Jahnatek, R. V. Chepulskii, R. H. Taylor, S. Wang, J. Xue, K. Yang, O. Levy, M. Mehl, H. T. Stokes, D. O. Demchenko and D. Morgan, *Comput. Mater. Sci.*, 2012, **58**, 218–226.

53 R. H. Taylor, F. Rose, C. Toher, O. Levy, K. Yang, M. Buongiorno Nardelli and S. Curtarolo, *Comput. Mater. Sci.*, 2014, **93**, 178–192.

54 G. Kresse and J. Hafner, *Phys. Rev. B: Condens. Matter Mater. Phys.*, 1993, **47**, 558–561.

55 C. E. Calderon, J. J. Plata, C. Toher, C. Oses, O. Levy, M. Fornari, A. Natan, M. J. Mehl, G. Hart, M. Buongiorno Nardelli and S. Curtarolo, *Comput. Mater. Sci.*, 2015, **108**(Part A), 233–238.

56 P. E. Blöchl, *Phys. Rev. B: Condens. Matter Mater. Phys.*, 1994, **50**, 17953–17979.

57 J. P. Perdew, K. Burke and M. Ernzerhof, *Phys. Rev. Lett.*, 1996, **77**, 3865–3868.

58 L. G. Ferreira, M. Marques and L. K. Teles, *Phys. Rev. B: Condens. Matter Mater. Phys.*, 2006, **74**, 075324.

59 M. Marques, L. K. Teles and L. G. Ferreira, *Phys. Rev. B: Condens. Matter Mater. Phys.*, 2007, **75**, 033201.

60 A. H. Cottrell, *An introduction to metallurgy*, St. Martin's Press, UK, 1967.

61 M. S. Darrow, W. B. White and R. Roy, *J. Mater. Sci.*, 1969, **4**, 313–319.